PNAS RESEARCH ARTICLE | CHEMISTRY ENVIRONMENTAL SCIENCES

Defining the challenges of Li extraction with olivine host: The roles of competitor and spectator ions

Gangbin Yan[a], Mingzhan Wang[a], Grant T. Hill[a], Siqi Zou[a], and Chong Liu[a,1]

Edited by Alexis Bell, University of California, Berkeley, CA; received January 14, 2022; accepted May 29, 2022

The lithium supply issue mainly lies in the inability of current mining methods to access lithium sources of dilute concentrations and complex chemistry. Electrochemical intercalation has emerged as a highly selective method for lithium extraction; however, limited source compositions have been studied, which is insufficient to predict its applicability to the wide range of unconventional water sources (UWS). This work addresses the feasibility and identifies the challenges of Li extraction by electrochemical intercalation from UWS, by answering three questions: 1) Is there enough Li in UWS? 2) How would the solution compositions affect the competition of Li^+ to major ions ($Na^+/Mg^{2+}/K^+/Ca^{2+}$)? 3) Does the complex solution composition affect the electrode stability? Using one-dimensional olivine $FePO_4$ as the model electrode, we show the complicated roles of major ions. Na^+ acts as the competitor ion for host storage sites. The competition from Na^+ grants Mg^{2+} and Ca^{2+} being only the spectator ions. However, Mg^{2+} and Ca^{2+} can significantly affect the charge transfer of Li^+ and Na^+, therefore affecting the Li selectivity. We point to improving the selectivity of Li^+ to Na^+ as the key challenge for broadening the minable UWS using the olivine host.

electrochemical Li extraction | olivine $FePO_4$ | unconventional water sources | competitor and spectator ions | intercalation

Significance

With the rapid market penetration of electric vehicles, securing lithium supply has become increasingly critical. However, the traditionally used lime–soda evaporation process is time-consuming, chemical-intensive, and applicable solely to concentrated Li brines. Electrochemical intercalation has emerged as a highly selective method, which enables Li extraction from more dilute unconventional water sources (UWS), including oil- and gas-produced water, geothermal brines, and rejected brines from seawater desalination. Here, with an $FePO_4$ model host, we reveal the different roles of major ions in Li competition and define that the key challenge to realizing Li mining from UWS and broadening minable sources is to improve the Li^+ to Na^+ selectivity, which can be achieved via further EDL and host materials design.

Lithium demand is estimated to increase by more than 30% per annum by 2030 (1, 2), driven by the growth of lithium-ion batteries for electric vehicles. Commercial lithium is mainly produced from land-based resources such as continental brines and high-grade ores using chemical processes that are time-consuming, energy- and chemical-intensive. These processes are technically and economically feasible only when the lithium concentration is around hundreds of parts per million (3–6). Therefore, to secure the Li supply and avoid the depletion of continental resources, identifying alternative resources and developing new mining methods are two critical solutions. Unconventional water sources (UWS), including oil- and gas-produced water (UOG), geothermal brines (Geo), and rejected brines from seawater desalination (Desal), contain untapped large quantities of Li. If used for Li mining, the existing infrastructure, such as pumps and wells, can be taken advantage of. However, a critical difference of UWS compared to continental brine is that the Li^+ concentration can be orders of magnitude lower. Direct extraction, which removes Li from the aqueous phase without disturbing the water sources, would be ideal for Li extraction from UWS to avoid extensive pretreatments and chemical usage.

Electrochemical intercalation has great potential to achieve direct Li extraction from UWS, owing to its working principles. Separating Li^+ from Na^+, K^+, Mg^{2+}, and Ca^{2+} simultaneously requires different mechanisms due to the nature of these ions, including their ionic and hydrated radii, charges, and hydration enthalpies (Fig. 1*A* and *SI Appendix*, Table S1) (7, 8). Here we choose one-dimensional (1D) olivine $FePO_4$ as the model host to illustrate the mechanism for Li separation. The selection of 1D olivine $FePO_4$ is due to its appropriate operating potentials, structure stability, thermodynamic Li preference, and low Li migration barrier (9–13). As shown in Fig. 1*B*, the selectivity of electrochemical intercalation comes from two main aspects. At the electrical double layer (EDL), dehydration and charge transfer occur, which is the first step to induce selectivity. Limited by the channel dimensions of the $FePO_4$ host (Fig. 1*C*) (14, 15), all ions need to be fully dehydrated before intercalation. Li^+ to Mg^{2+} and Ca^{2+} selectivity can be achieved due to the significant differences in their hydration enthalpies. In the second step, ions need to migrate in the crystalline host materials and be stored in the interstitial sites. Li^+ intercalation is favored over Na^+, K^+, Mg^{2+}, and Ca^{2+} in 1D $FePO_4$ host, owing to its stronger bonding or much smaller migration barrier (Fig. 1*D* and *SI Appendix*, Table S2) (10, 16, 17). These two steps, involving both the thermodynamic and kinetic factors, govern Li selectivity to all the major ions. However, whether this level of Li preference can conquer orders of magnitude concentration difference in UWS is unknown.

Author affiliations: [a]Pritzker School of Molecular Engineering, University of Chicago, Chicago, IL 60637

Author contributions: G.Y. and C.L. designed research; G.Y. performed research; G.Y., M.W., G.T.H., and S.Z. contributed new reagents/analytic tools; G.Y. and C.L. analyzed data; and G.Y., M.W., G.T.H., S.Z., and C.L. wrote the paper.

The authors declare no competing interest.

This article is a PNAS Direct Submission.

[1]To whom correspondence may be addressed. Email: chongliu@uchicago.edu.

This article contains supporting information online at http://www.pnas.org/lookup/suppl/doi:10.1073/pnas.2200751119/-/DCSupplemental.

Published July 25, 2022.

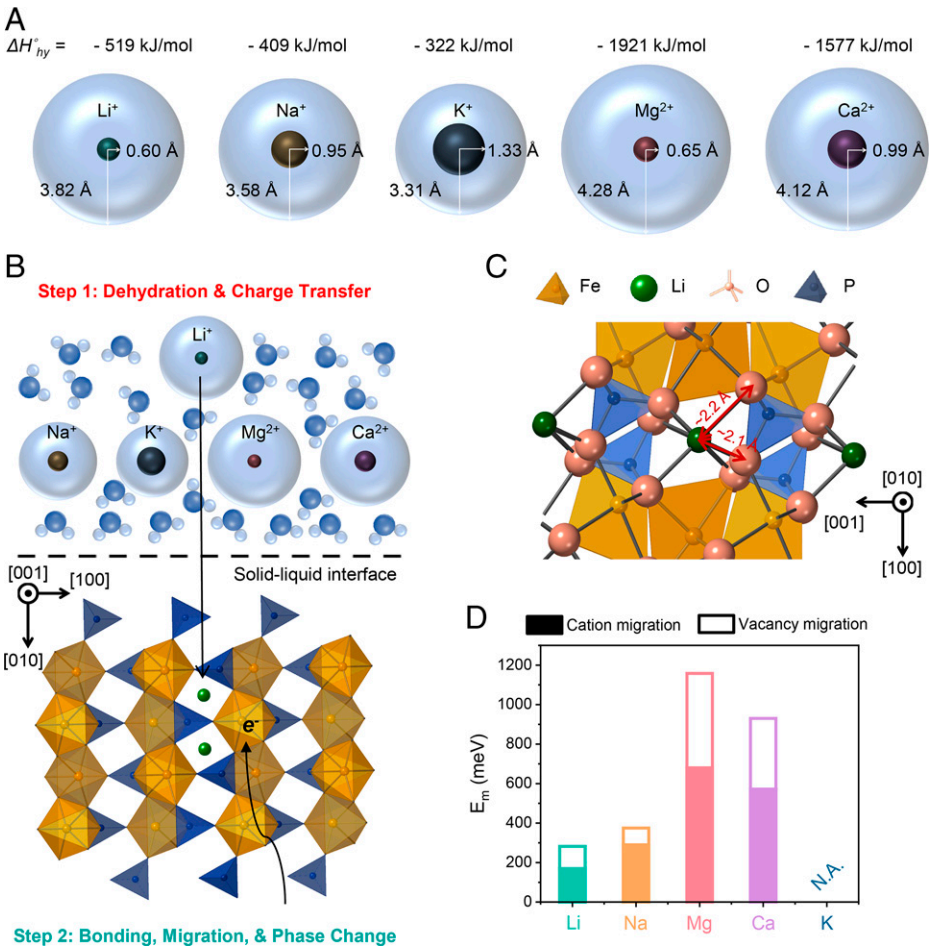

Fig. 1. Properties of the main ions and working principles of electrochemical intercalation to induce Li selectivity. (*A*) Schematic showing hydration enthalpies and ionic and hydrated radii of Li^+, Na^+, K^+, Mg^{2+}, and Ca^{2+}. (*B*) Schematic showing the solid–liquid interface during electrochemical intercalation. Ions are fully dehydrated before entering the crystal structure of $FePO_4$. Two steps are involved in inducing Li selectivity. (*C*) The crystal structure of $LiFePO_4$ projected along the [010] direction, with Li–O interatomic distances labeled. (*D*) Migration barriers for cations in charged hosts and vacancy in discharged hosts from density functional theory calculation, adapted from refs. 10, 16, and 17 (N.A. denotes no reported value for K^+/vacancy migration in the host).

To address the feasibility and effectiveness of Li mining from UWS by electrochemical intercalation, three key questions must be answered. First, can a significant amount of Li be extracted from UWS? Second, how does Li selectivity depend on the UWS composition, such as which ion competes with Li^+ at what conditions? Specifically, UWS have wide ranges of Li^+ concentrations from 0.001 ppm to 1,000 ppm, and the solution composition is complex, with hundreds and thousands of times more concentrated major ions (i.e., Na^+, Mg^{2+}, Ca^{2+}, and K^+, among others). Despite intriguing proof-of-concept works on electrochemical intercalation-based Li^+ extraction, most tests are done in simplified binary electrolytes, such as Li–Na or Li–Mg, simulated continental brines, and seawater, which can only reflect a small spectrum of UWS (11, 13, 18–24). The third question is about stability: Would the composition complexity pose an electrode stability challenge even in ideal cases where the Li Faradaic efficiency (FE_{Li}) is approaching 100%?

This work addresses all the above key questions. We first estimate the potential annual Li production from UWS and categorize UWS by the Li^+ concentration with respect to Na^+, K^+, Mg^{2+}, and Ca^{2+} concentrations based on more than 122,000 water sources. Second, to understand the effects of mixed electrolyte composition, we study the host behaviors in unary, binary, ternary, and quaternary solutions. We show that the competition is determined by the EDL composition and structure, which cannot be directly predicted by the thermodynamics and kinetics in unary systems. Depending on whether competing for storage sites, we divide the main ions into two groups: competitor ion (Na^+) and spectator ions (K^+, Mg^{2+}, and Ca^{2+}). Mg^{2+} and Ca^{2+} as the spectator ions, even not directly competing with Li^+ for host storage sites, will significantly change the charge transfer property of Li^+, therefore affecting the Li selectivity. The presence of Na^+ can lower the Li charge transfer barrier, however, decreasing the Li selectivity. Finally, we address the stability question by realizing the longest extraction cycle life with olivine $FePO_4$ hosts, using the simulated Atacama brine. The Faraday efficiency of Li (FE_{Li}) is maintained at 100% ± 2.5% for 100 extraction cycles (14.7 mA/g with 73.5 mAh/g capacity usage), without obvious selectivity decay. Therefore, if not intercalated, major ions will not pose stability issues. This work identifies the current minable UWS and highlights that improving Li^+ to Na^+ selectivity is the key to broadening the minable UWS with 1D olivine hosts.

Results and Discussion

Estimation of Li Production from UWS and Classification of the Sources. In Fig. 2*A*, we first summarize the estimated annual Li production from many UWS in the United States and globally (assuming a 90% recovery). Annually, US UOG alone can provide nearly 3 times the global Li consumption in 2019. US Geo and global Desal also contain significant Li

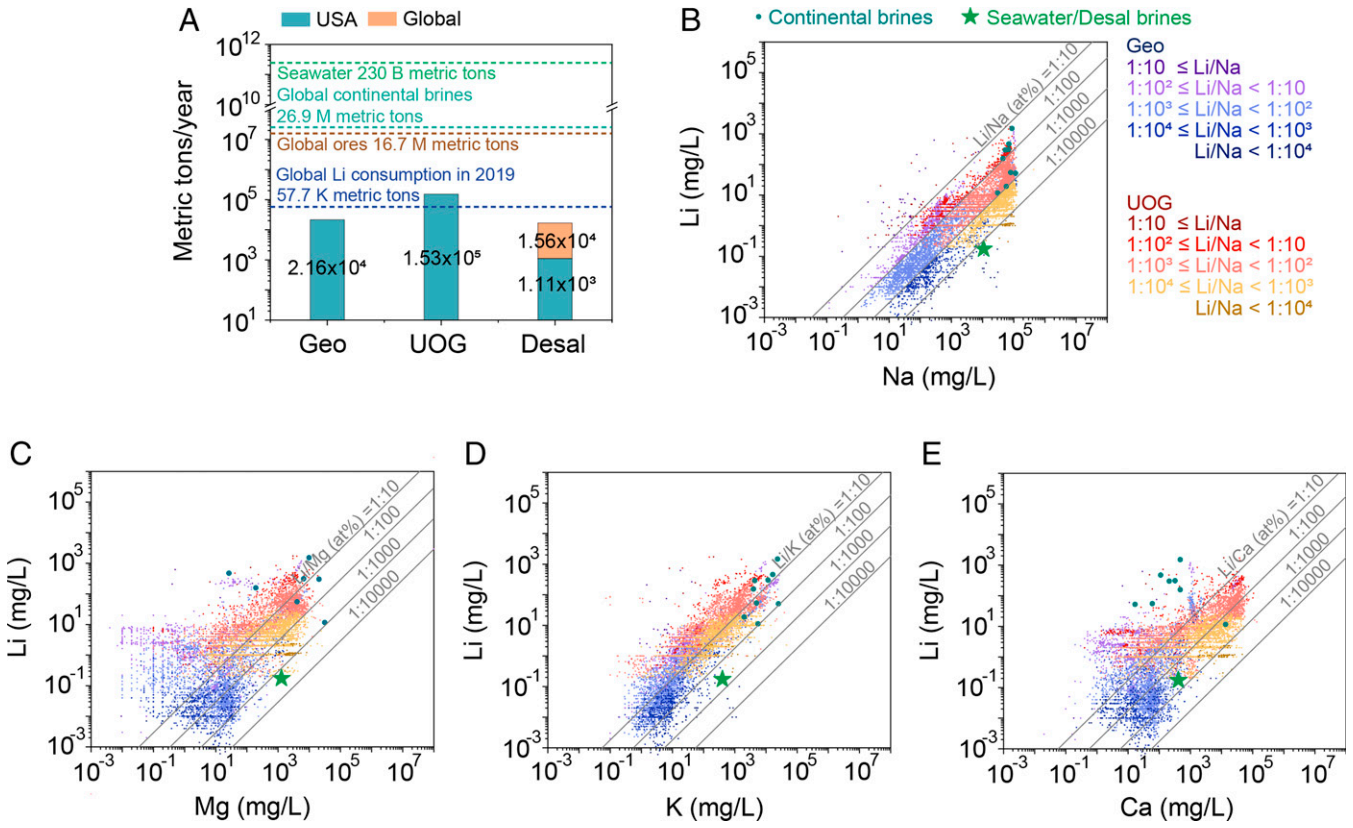

Fig. 2. Estimated Li production from UWS and classification of UWS by compositions. (*A*) Estimated Li annual production from UWS in the United States and the globe, all assuming a 90% recovery. For US Geo, annual lithium throughput was ~24,000 t in 2019, reported in a US Department of Energy report (25); for US UOG, the estimated value is calculated from a median of Li^+ concentration (44 mg/L), reported in an Environmental Protection Agency report (26), and the total volume of UOG in the United States (2.8 billion gallons per d in 2017), reported in an National Ground Water Research and Educational Foundation report (27); for Desal, the estimated value is calculated from a seawater Li^+ concentration (~0.2 ppm) (12, 13), and the total volume of processed water (brine and desalinated water) in the United States (16.94 million m^3/d) and the globe (236.87 million m^3/d) (28). (*B–E*) Li^+ concentration with respect to the concentrations of Na^+, Mg^{2+}, K^+, and Ca^{2+} in continental brines (29), Geo/UOG in the United States [USGS source (30, 31)], and seawater/Desal water (12, 13). Each source was first categorized into different groups according to the Li–Na molar ratio, with color coding. Then the same color code is used for the other Li–Mg/K/Ca plots. Li–M equimolar ratio reference lines are also labeled in gray.

amounts, equivalent to ~37% and 27% of 2019 global consumption. These results show the feasibility of supplying Li from mining UWS. For electrochemical intercalation, both Li^+ concentration and the ratio of Li^+ to major ions affect the Li selectivity. Therefore, in Fig. 2*B–E*, based on the US Geological Survey (USGS) database of US UOG and US Geo, we have summarized the Li^+ concentrations and molar ratios with respect to the major ions (M = Na^+, Mg^{2+}, K^+, and Ca^{2+}), considering more than 122,000 water sources. This categorization clearly shows the UWS quality for Li mining, with high-quality UWS containing both high Li^+ concentrations and high Li^+ ratios. UWS have wide ranges of Li concentrations. Some UWS have much lower Li^+ concentrations than that in continental brines, and the competition from major ions is also stronger. In terms of the molar ratios, the Li/Na molar ratio shows the widest range (1:10 to ~1:20,000), while K is less competitive, with Li/K higher than 1:100 for most sources. Interestingly, Li–Mg and Li–Ca (Fig. 2*C* and *E*) show similar distribution patterns, with Li/Mg or Li/Ca in most sources higher than 1:1,000. Besides, US UOG is of higher quality for Li extraction than US Geo or Desal, based on the Li^+ concentration. To have a complete picture, we also summarized the Na–Mg, Na–Ca, and Mg–Ca concentrations/molar ratios in *SI Appendix*, Fig. S1. Based on the Li–M molar ratios, Na^+ is the dominant ion, followed by Ca^{2+}, Mg^{2+}, and K^+. However, it is worth noting that there are cases when Mg^{2+} or Ca^{2+} have higher concentrations than Na^+.

Unary (PureM) System Thermodynamics and Kinetics. Electrochemical intercalation behavior in the unary system provides information about the thermodynamics and kinetics of each ion, which is a good indicator for Li selectivity. We first compared the intercalation of pure Li^+, Na^+, Mg^{2+}, Ca^{2+}, or K^+ into $FePO_4$ hosts (Fig. 3*A* and *B*). Fig. 3*A* shows the cyclic voltammetry (CV) results for $FePO_4$ in 1 M cation solutions under a slow scan rate (0.03 mV/s). The CV scan of $FePO_4$ in 1 M LiCl aqueous solution shows a pair of symmetric anodic and cathodic peaks, with half-wave potential ($E_{1/2}$ = 0.208 V vs. Ag/AgCl) close to the thermodynamic value (3.45 V vs. Li/Li^+ = 0.213 V vs. Ag/AgCl) (32, 33). In 1 M NaCl aqueous solution, two well-defined current peaks are found for the anodic process, and only one current peak is observed for the cathodic scan. This asymmetric behavior is due to the formation of the $Na_{0.7}FePO_4$ intermediate phase during the charging process (34, 35). Meanwhile, in 1 M $MgCl_2$ (aq) solution, although a sharp cathodic peak is observed at −0.46 V vs. Ag/AgCl, a broad anodic wave is observed at −0.18 V. The large peak-to-peak separation, as well as a significant difference between the cathodic and anodic peaks, suggests sluggish kinetics and irreversibility of the Mg^{2+} (de)intercalation. Besides, the value of the current peak in LiCl (aq) is more than 3 times higher than that in NaCl (aq) or $MgCl_2$ (aq) at the same scan rate, which demonstrates faster kinetics of Li^+ insertion and extraction in $FePO_4$ hosts. In sharp contrast, we barely see redox peaks in 1 M KCl and $CaCl_2$ (aq) solutions within the

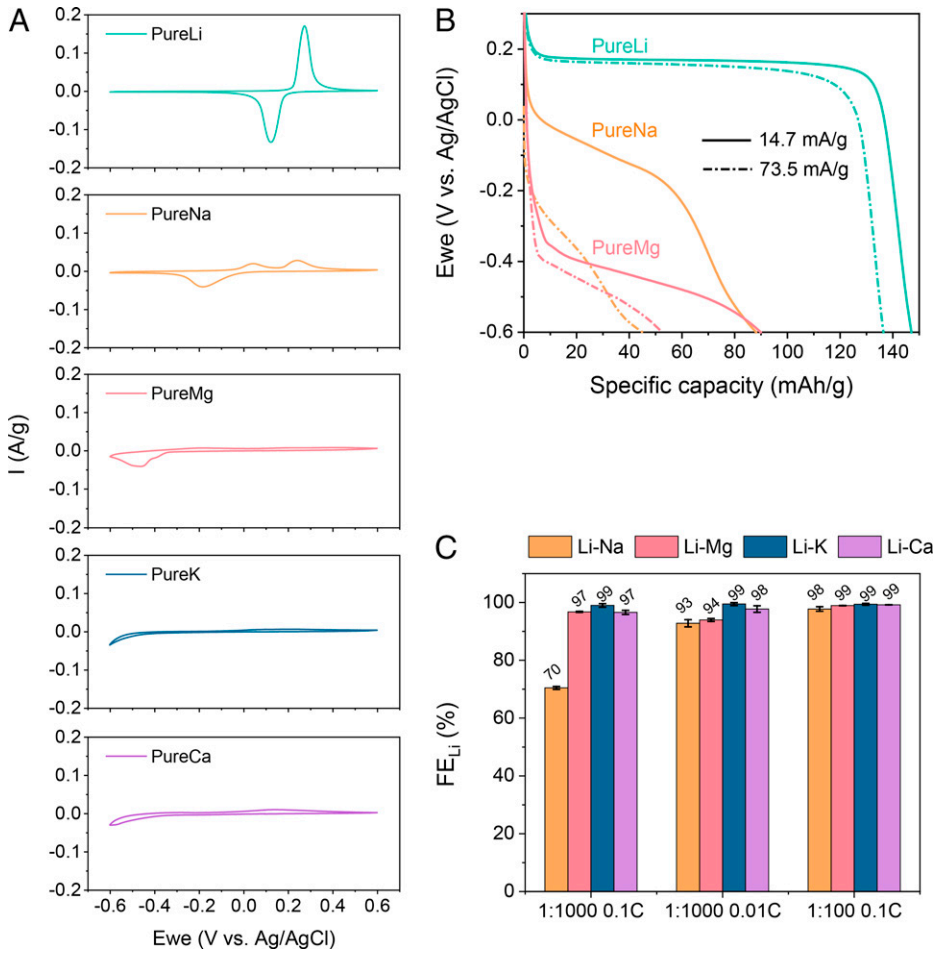

Fig. 3. Performance in unary (PureM) and binary (Li–M1) solutions. (*A*) CV tests for $FePO_4$ host in 1 M pure Li/Na/Mg/K/Ca chloride aqueous solution at a 0.03 mV/s scan rate. (*B*) CP intercalation curves in 1 M pure $Li^+/Na^+/Mg^{2+}$ chloride aqueous solution under 0.1 C and 0.5 C (14.7 mA/g equals a rate of 0.1 C; Ewe denotes the potential of the working electrode versus Ag/AgCl/saturated KCl reference electrode; *SI Appendix*, Fig. S3). (*C*) Faraday efficiency of Li extraction in binary (Li–Na/Mg/K/Ca) solutions with different molar ratios and different extraction C rates (error bars represent the SD of three replicate measurements; $[Li^+]$ is kept at 1 mM).

selected voltage window, especially in KCl (aq), indicating no ion (de)intercalation process was involved. This could be attributed to the large ionic radii and migration barriers of K^+ and Ca^{2+} (Figs. 1*A* and *D* and 3*A* and *SI Appendix*, Tables S1 and S2) (7, 16, 17). We also conducted chronopotentiometry (CP) tests at slow and fast rates. As shown in Fig. 3*B*, at a slow C rate of 0.1 C (14.7 mA/g), $FePO_4$ experienced the smallest overpotential during Li^+ intercalation and the largest overpotential during Mg^{2+} intercalation, compared with the calculated thermodynamic voltage (*SI Appendix*, Table S3). Moreover, at increased C rates (0.5 C or 73.5 mA/g), there is a big overpotential difference during Na^+ intercalation, and a small difference during Li^+ intercalation, indicating the preference of Li^+ intercalation and sluggishness of Na^+ migration. Interestingly, the overpotential difference at increased kinetics during Mg^{2+} intercalation is small, showing that the charge transfer at the interface rather than migration could be the rate-limiting step (36, 37). The unary results reveal the potential of the $FePO_4$ host to have high Li selectivity to all the major ions based on the intercalation thermodynamics and kinetics.

Li Selectivity in Binary (Li–M1) Solutions. Next, we study the Li selectivity in binary (Li–M1) solutions. The Faraday efficiencies of Li (FE_{Li}) are summarized in Fig. 3*C*. In a Li–M1 molar ratio of 1:100 and 0.1 C, Li showed $FE_{Li} > 98\%$ for all the cases. For 1:1,000 Li–Na/Mg/K/Ca, FE_{Li} are 93% ± 1.2% ($\eta_{Li\text{-}Na} = 1.3 \times 10^4$), 94% ± 0.5% ($\eta_{Li\text{-}Mg} = 3.1 \times 10^4$), 99% ± 0.5% ($\eta_{Li\text{-}K} = 9.9 \times 10^4$), and 98% ± 1.1% ($\eta_{Li\text{-}Ca} = 9.8 \times 10^4$) under 0.01 C. At a faster rate of 0.1 C, the FE_{Li} are 97% ± 0.2%, 99% ± 0.6%, and 97% ± 0.7% in Li–Mg/K/Ca binary systems. This supports the difficulties of $Mg^{2+}/K^+/Ca^{2+}$ intercalation into $FePO_4$ hosts, and these ions behave like spectators instead of competing for host storage sites. However, under 0.1 C at a 1:1,000 molar ratio of Li–Na, FE_{Li} decreased significantly to 70% ± 0.5% ($\eta_{Li\text{-}Na} = 2.3 \times 10^3$). In this case, Na was identified as a strong competitor. Apparently, the single-component thermodynamics and kinetics cannot explain the competition between Li and Na at 0.1 C under a 1:1,000 molar ratio. We can see, from Fig. 3*B*, that the intercalation plateau voltage difference at 0.1 C between Li^+ and Na^+ is >0.3 V. Such a high voltage difference is equivalent to an approximately five orders of magnitude concentration Nernstian shift. However, the Na^+ starts to compete with Li^+ at only three orders of magnitude higher concentration. It is intuitive that, with orders of magnitude higher concentration of Na^+ in the solution, the electrical double layers will be dominated by Na^+ ions. Therefore, the charge transfer resistance of Li^+ will change, and the Nernstian shift can no longer predict the intercalation voltage, which is also reflected in the CP intercalation potential of $FePO_4$ hosts in the 1:1,000 Li–Na (aq) solution (*SI Appendix*, Fig. S4). Since, for authentic brines, some other anions may also be present, such as NO_3^- and SO_4^{2-}, and the

concentration of major ions and Li^+ can vary in different brines, while the Li molar ratio is the same (Fig. 2), we further tested the anion and concentration effects on Li selectivity. As shown in *SI Appendix*, Fig. S5, we tested Li extraction performance in 1:1,000 Li–Na/Mg/K/Ca solutions with two other different anions (NO_3^- and SO_4^{2-}) under 0.1 C. Na^+ still behaves as the main competitor to Li^+ in nitrate and sulfate solutions (~70% FE_{Li}). Meanwhile, Li showed FE_{Li} > 92% in 1:1,000 Li–Mg/K/Ca nitrate or sulfate binary solutions, and the slight performance difference compared to that in chloride solutions may be due to the variation of solution features, such as the activity coefficient of the solutes, ionic strength, and EDL structures (38). $CaSO_4$ is not included, due to the solubility limit. For the concentration-dependent Li selectivity tests in 1:1,000 Li–Na/Mg/K/Ca binary solutions, as shown in *SI Appendix*, Fig. S6*A*, at a fixed Li^+ to Na^+ ratio of 1:1,000, the FE_{Li} increased with the Li concentration. Specifically, the FE_{Li} increases to 83% ± 0.4% if there is 2 mM Li^+ in the Li–Na solution. However, with 0.1 mM Li^+ in Li–Na binary solution, the FE_{Li} is only 34% ± 0.5%. Meanwhile, in 2 mM:2 M Li–Mg/K/Ca binary systems, Li still maintained high FE_{Li} > 95%. However, we witnessed a significant mismatch between the used capacity and the capacity measured from the recovered ions in the cases of 0.1 mM:0.1 M Li–Mg/K/Ca binary solutions (*SI Appendix*, Fig. S6*A*). At such a low [Li^+] (0.1 mM), the limiting diffusion current of Li^+ becomes important (11, 39). For the Li–Na binary system, insufficient current flow will be supplemented by the current of sodium ions, which helps prevent other sides reactions of hosts but decreases the Li selectivity. However, for the Li–Mg/K/Ca binary solutions, the large (~70%) intercalation capacity is probably associated with irreversible processes such as surface degradation or amorphization reactions of the $FePO_4$ hosts (36, 37, 40), since Mg^{2+}/K^+/Ca^{2+} are challenging to intercalate. This is also indicated by the low and flat CP intercalation regions in Li–Mg/K/Ca binary solutions (*SI Appendix*, Fig. S6*B*). For the majority of unconventional sources, Na^+ will still be the one with the highest concentration, which can help prevent irreversible reactions. When Mg^{2+} or Ca^{2+} is dominating, identification of all the faradaic processes is necessary.

$FePO_4$ Host Behavior in Ternary (Li–M1–M2) and Quaternary (Li–M1–M2–M3) Solutions and Simulated Brines. The results from the binary competition reveal the importance of EDL composition, which is determined by the solution composition. To investigate the effect of solution composition on charge transfer resistance and intercalation voltage, we adopted step-concentration CP (Stepconc CP) tests (see *Materials and Methods* for more details). We probe the CP voltage profile during the change of Li molar ratio in either binary or ternary solutions while keeping the main interfering ion concentrations unchanged (1 M). As shown in Fig. 4*A*, we show the Stepconc CP (0.1 C) for Li–Na/Mg/Ca binary systems with ion molar ratio decreasing from 1:100 to 1:1,000 ([Na^+]/[Mg^{2+}]/[Ca^{2+}] is kept at 1 M). For all cases, the intercalation potential decreases as the Li ratio decreases. However, the intercalation potentials do not follow the Nernstian shift based on Li^+ concentrations. Especially, a jump in potential decrease was observed for both Li–Mg (>0.27 V) and Li–Ca (>0.18 V) systems at a Li^+ to Mg^{2+} or Ca^{2+} ratio of 1:600. Based on our previous inductively coupled plasma mass spectrometry (ICP-MS) results (Fig. 3*C*) of the Li–Mg and Li–Ca systems, at a Li^+ to Mg^{2+} or Ca^{2+} ratio as low as 1:1,000, the FE_{Li} is still above 97%, which means that the large drop of voltage is due to the overpotential increase of Li^+ intercalation. The explanation of the large Li^+ charge transfer resistance is shown in Fig. 4*C* using the Li–Mg system. At a high Li–Mg molar ratio (such as 1:100), the intercalation voltage of Li^+ only deviates slightly from the Nernstian behavior (Fig. 4*A*), owing to the loose EDL network. However, when the Li–Mg molar ratio decreases to a threshold value (e.g., 1:600), the increased coverage of Mg^{2+} ions at the EDL could induce rigid water structures and strengthened screening effect, both of which will result in much larger Li^+ charge transfer resistance (41–44). As a result, even though Mg^{2+} and Ca^{2+} do not compete for the storage sites, they will significantly increase the intercalation energy barrier for Li^+ at low Li^+ to Mg^{2+}/Ca^{2+} molar ratio. The large non-Nernstian potential jump caused by the existence of Mg^{2+} allows Na^+ to have enough energy to overcome its intercalation barrier (Fig. 4*A* and *SI Appendix*, Fig. S7), which indicates the possibility of Na^+ competition. Moreover, we tested two conditions in the Li–Na–Mg–Ca quaternary system. For example, with the same Li^+ (1 mM), Na^+ (100 mM or 1 M), and total divalent ion ([Mg^{2+}] + [Ca^{2+}] = 1 M) concentrations, FE_{Li} in 1:100:500: 500 Li–Na–Mg–Ca quaternary solution is 10% lower than that in 1:100:1,000 Li–Na–Mg ternary solution (*SI Appendix*, Fig. S8). Meanwhile, as shown in *SI Appendix*, Fig. S9, the non-Nernstian jump is more significant. The increased overpotential promotes the intercalation of Na^+, which corroborates with the decreased FE_{Li} we have measured. This again demonstrates the complex effect of solution compositions on the charge transfer of Li^+ and Na^+. The results follow the characteristics of Mg^{2+} and Ca^{2+} as spectator ions.

We then tested the Li selectivity for Li–Na–Mg/Ca ternary systems, to probe the effect of spectator ions (Mg^{2+} and Ca^{2+}) on the competition between Li^+ and Na^+. As shown in Fig. 4*B*, with the Li^+ to Mg^{2+} ratio right before the large non-Nernstian jump (Li^+ to Mg^{2+} of 1:600), the FE_{Li} was maintained at 98% ± 0.3% for the 1:100:500 Li–Na–Mg ternary solution. However, as predicted by the Stepconc CP, with the Li^+ to Mg^{2+} ratio below the large non-Nernstian jump (e.g., 1:100:1,000 Li–Na–Mg), the FE_{Li} experienced a significant decrease to only 85% ± 0.01%. Similar results were observed for the Li–Na–Ca ternary system. The FE_{Li} was maintained at 98% ± 0.4% for the 1:100:500 Li–Na–Ca ternary solution, with Li^+ to Ca^{2+} before the large non-Nernstian jump (Li^+ to Ca^{2+} of 1:600). As expected, the FE_{Li} in 1:400:1,000 Li–Na–Ca ternary solution decreased to 83% ± 0.8%. The decrease of FE_{Li} is due to Na^+ intercalation into the storage sites. These results reveal the important roles of spectator ions, Mg^{2+} and Ca^{2+}, in controlling the charge transfer at the electrical double layer to affect the Li^+ to Na^+ selectivity.

Even though the predicted Na^+ competition was validated, it is interesting that, in these ternary system tests, Li^+ still showed stronger competitiveness than Na^+ despite its lower intercalation voltage in the Li–Mg and Li–Ca binary systems (at Li^+ to Mg^{2+} or Ca^{2+} ratio below 1:600) than Na^+ (for 1 M Na^+ at 0.1 C). For example, FE_{Li} in 1:600: 600 Li–Na–Mg is 81% ± 0.9%, with Li and Na filling ratios of 81% and 19%. To explain this phenomenon, another Stepconc CP test was conducted. As shown in *SI Appendix*, Fig. S10, we changed the concentration of the solution from 1: 600 Li–Mg to 1:600:600 Li–Na–Mg at the final step, while keeping [Li^+] the same at 1.67 mM. As Na^+ was added to the solution, a significant decrease in intercalation overpotential was observed. We attribute this decrease to the loosened EDL water network and the decreased surface charge density caused by the Na^+ intercalation reactions (Fig. 4*C*). Therefore, the existence of Na^+ can facilitate the insertion of Li^+ at smaller overpotential, which prevents Mg^{2+}, K^+, and Ca^{2+} from competing for the storage

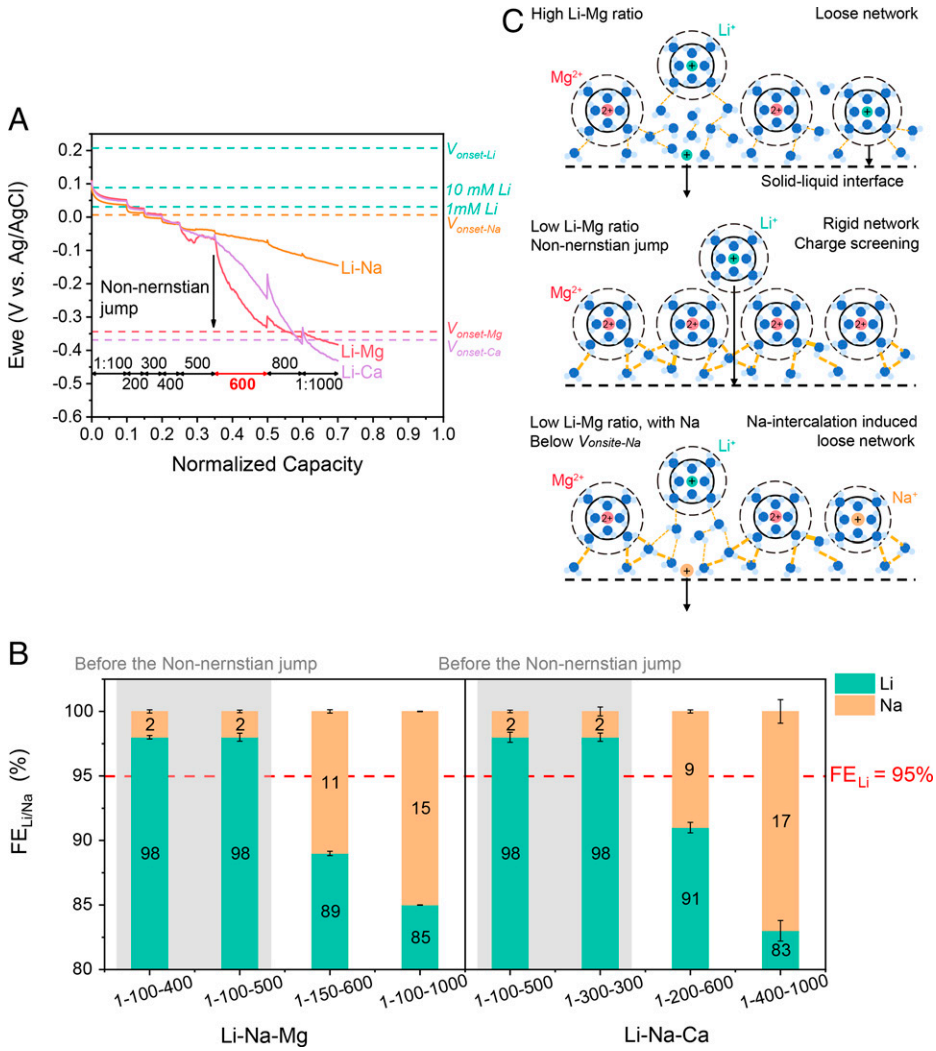

Fig. 4. Stepconc CP tests and host behavior in ternary solutions. (*A*) Stepconc CP tests in Li–Na/Mg/Ca binary systems with decreasing Li ratio from 1:100 to 1:1,000 ($[Na^+]/[Mg^{2+}]/[Ca^{2+}]$ is kept at 1 M; see *Materials and Methods* for more details; $V_{onset\text{-}Li/Na/Mg/Ca}$ are acquired from the onset potential of the cathodic current peak during CV scan in Fig. 3*A*; 10 mM and 1 mM Li denote the Nernstian potential shift corrected by Li^+ concentration change). (*B*) Faraday efficiency of Li (green) or Na (orange) in Li–Na–Mg or Li–Na–Ca ternary systems ($[Li^+]$ is kept at 1 mM), calculated from ICP-MS recovery results. (*C*) Schematic showing different EDL structures induced by different compositions.

sites or damaging the host structure, although at a penalty of decreased Li^+ to Na^+ selectivity. To further verify whether a reaction is necessary for the reduction of intercalation overpotential, we conducted another Stepconc CP test in the Li–Ca–K ternary system. At the final step, we changed the concentration of the solution from 1:600 Li–Ca to 1:600:600 Li–Ca–K, while keeping $[Li^+]$ the same at 1.67 mM (*SI Appendix*, Fig. S11). Interestingly, the response is quite different from that with the addition of Na^+ (*SI Appendix*, Fig. S10). Although we also observed a decrease in overpotential immediately after the addition of K^+, the slope of the Stepconc CP curve did not change, and the potential would go back to the original level. This again demonstrates the spectator behavior of K^+ ions and proves the necessity of the reaction. However, whether an intercalation reaction is necessary compared to solution redox reactions is unknown and is worth future investigation.

Due to the complex effect of EDL on the charge transfer of Li^+ and Na^+, binary electrochemical intercalation behavior cannot directly predict Li^+ to Na^+ selectivity in the ternary system. To evaluate the FE_{Li} throughout the ternary concentration range, we used ordinary least square (OLS) regression (see *Materials and Methods* for more details; Fig. 5*A* and *B*) based on the experimentally sampled Li selectivity in ternary systems with different compositions. For all the sampled conditions, the competition for the storage sites comes from Na^+, while Mg^{2+} or Ca^{2+} behaves as a spectator ion. Increasing the Mg^{2+} or Ca^{2+} concentration in the Li–Na system would lead to a decrease of Li selectivity. Near the diagonal lines, where Na^+ and Mg^{2+} or Ca^{2+} have similar concentrations (such as 1:1,000:1,000), the selectivity of Li^+ was the lowest compared to either Li–Na or Li–Mg/Ca binary systems of the same molar ratio. Moreover, the Li selectivity still depends more on the Li^+ to Na^+ ratio in the system. The evaluation of regression accuracy is provided in *SI Appendix*, Fig. S12.

We highlighted, in Fig. 5*A* and *B*, the solution compositions with $FE_{Li} > 95\%$, which have the potential to be utilized for direct Li mining with 1D $FePO_4$ electrodes without much material or method optimization. We also labeled 11 continental brines in the ternary selectivity diagrams (see *SI Appendix*, Table S4 for detailed brine compositions). We validated the Li selectivity in three simulated brines, resembling the compositions of Taijinaier in China, Atacama in Chile, and Dead Sea in Israel. Since the Mg^{2+} molar ratio in these three brines is higher than the

Ca^{2+} molar ratio, we put these three data points into the Li–Na–Mg ternary solution map. And the corresponding experimental selectivities are 100% ± 1.2%, 100% ± 1.1%, and 78% ± 3.5%. The tested values align with the predicted values by OLS regression.

Finally, we addressed the question about the stability of 1D $FePO_4$ hosts in complex solutions. We achieve the longest extraction cycle life with $FePO_4$ hosts, using the simulated Atacama brine as the source. The FE_{Li} is maintained at 100% ± 2.5% for 100 cycles, without significant selectivity decay (Fig. 5*C*). *SI Appendix*, Fig. S13 *A* and *B* show the constant current intercalation (14.7 mA/g) curves in the simulated Atacama brine and the deintercalation (3.675 mA/g) curves in the 30 mM NH_4HCO_3 recovery solutions, respectively. Specifically, for the deintercalation side, the final potential difference between the 10th and 100th deintercalation is 0.14 V, which is only 0.04 V for the intercalation side. These results show that, if not intercalated, major ions will not pose threats to stability. Therefore, improving the Li^+ to Na^+ selectivity will allow the 1D $FePO_4$ hosts be used for more challenging UWS with lower Li^+ concentrations and Li^+ molar ratios.

Conclusions

In conclusion, we verified the feasibility of Li production from UWS and categorized UWS using their compositions, considering more than 122,000 sources. Furthermore, through systematically studying the host's behavior in unary, binary, ternary, and simulated brines, we discussed the competitiveness of the main interfering ions (Na^+, K^+, Ca^{2+}, and Mg^{2+}) for Li^+ extraction. Na^+ is identified as the dominant competitor ion to Li^+. The divalent ions, Mg^{2+} and Ca^{2+}, are identified as spectator ions. They do not directly compete for host storage sites but can significantly affect the Li^+ to Na^+ selectivity by altering the EDL structures. K^+ is inert for intercalation and of lower concentration than Na^+, Ca^{2+}, and Mg^{2+} in UWS, therefore being the spectator ion with the least effect on Li selectivity. Finally, we addressed the stability question by achieving the longest extraction cycle life in simulated Atacama brine, with FE_{Li} maintained at 100% ± 2.5% for 100 extraction cycles. This work points to improving the selectivity of Li^+ to Na^+ as the key challenge for broadening the minable UWS using the olivine host.

Materials and Methods

Synthesis of $FePO_4$ Microplatelets. To synthesize pristine $LiFePO_4$ microplatelets, a solvothermal method with mixed water and polyethylene glycol solvent was used, modified from the previous report (45). All the operations were done in an N_2/H_2O glovebox to ensure that all precursors were not exposed to oxygen. Six milliliters of 0.2 M $H_3PO_{4(aq)}$ was mixed with 24 mL of polyethylene glycol 400. Afterward, 18 mL of 0.2 M $LiOH_{(aq)}$ was added to create the creamy white Li_3PO_4 precipitate. This mixture was stirred in an N_2 glovebox overnight to remove dissolved oxygen. Next, 1.2 mmol of $FeSO_4{\cdot}7H_2O$ was dried under vacuum in a Schlenk line overnight, while 12 mL of H_2O was stored in the N_2 glovebox for deoxygenation. Next, the deoxygenated H_2O was transferred to the dried $FeSO_4$ powder and stirred for about 10 min, creating a lime green solution. The $FeSO_4$ solution was transferred to the Li_3PO_4 suspension without oxygen exposure, and the entire mixture was transferred to a 100-mL Teflon-lined autoclave. The autoclave was heated to 140 °C for 1 h, then to 210 °C for 17 h, and cooled. This procedure yields microsized $LiFePO_4$ platelet particles (*SI Appendix*, Fig. S14).

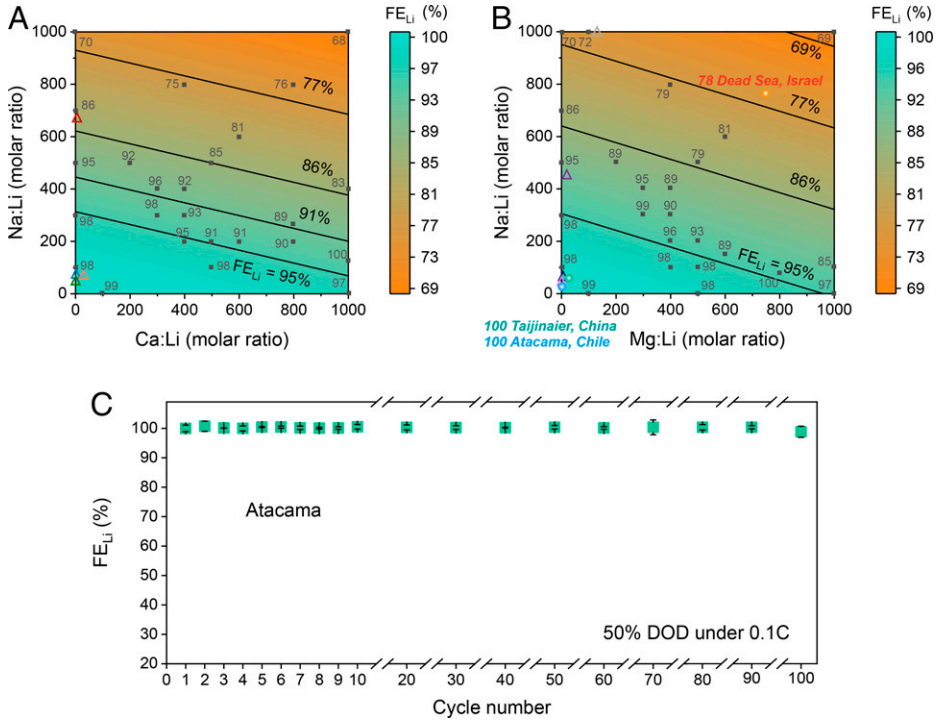

Fig. 5. Li extraction performance in ternary solutions and simulated brines. (*A*) Li selectivity in Li–Na–Ca ternary solution. (*B*) Li selectivity in Li–Na–Mg ternary solution. ([Li^+] is fixed at 1 mM for Li–Na–Mg/Ca ternary solutions, except for the simulated brines); compositions with the same FE_{Li} value are labeled in solid black reference lines; the gray squares denote the experimentally acquired FE_{Li} in different solutions (average FE_{Li} value of the replicate measurements used for the denotation), and the FE_{Li} color maps illustrate the predicted value with the use of OLS regression (all measured FE_{Li} from the replicate tests treated as independent data points for regression). The three open circles represent the three tested brines: green, Taijinaier in China; blue, Atacama in Chile; orange, Dead Sea in Israel. The open triangles denote the other brines listed in *SI Appendix*, Table S4: blue, Clayton Valley in the USA; red, Searles Lake in the USA; purple, Bonneville in the USA; black, Salar de Uyuni in Bolivia; green, Zabuye in China; orange, Salton Sea in the USA; gray, Great Salt Lake in the USA; pink, Hombre Muerto in Argentina. (*C*) Long-term Li extraction performance in simulated Atacama brine using 50% depth of discharge (DOD) under 0.1 C intercalation C rate (14.7 mA/g with 73.5 mAh/g capacity usage).

After the synthesis was completed, the white $LiFePO_4$ particles were centrifuged three times with deionized (DI) water and dried. Carbon coating was conducted by mixing the $LiFePO_4$ with sucrose at a mass ratio of 5:1 ($LiFePO_4$:sucrose) without breaking the primary particles. This sample was heated to 600 °C for 5 h in a tube furnace under flowing Ar to yield the carbon-coated $LiFePO_4$.

For chemical extraction of Li from carbon-coated $LiFePO_4$, an oxidizing solution was prepared by dissolving 1.36 g of nitronium tetrafluoroborate (NO_2BF_4) in 80 mL of acetonitrile. Then 0.8 g of carbon-coated $LiFePO_4$ powder was immersed into the solution and stirred for 24 h at room temperature. The powder was then washed several times by acetonitrile and finally dried in a vacuum oven for 12 h. Powder X-ray diffraction (XRD) confirms that both $LiFePO_4$ and $FePO_4$ are single phase (*SI Appendix*, Fig. S15).

Preparation of Electrodes. The $FePO_4$ electrodes were prepared by casting a slurry of $FePO_4$, Super P carbon black, and polyvinylidene fluoride with a mass ratio of 80:10:10, in *N*-methyl-2-pyrrolidone. The electrode slurry was drop cast on a 0.5×1 cm^2 geometrical surface of a carbon cloth (ELAT-H, FuelCellEtc) current collector of 5×1 cm^2 and dried on a hot plate at 100 °C overnight. During tests, the other end of the carbon cloth was connected to a Pt clamp. The active material mass loadings ranged between 7 and 14 $mg{\cdot}cm^{-2}$. $NaFePO_4$ counter electrodes were made with the same slurry depositing on carbon felt (Alfa Aesar) disks (0.9525 cm diameter × 3.18 mm thickness) by galvanostatically sodiating $FePO_4$ in 1 M $NaCl_{(aq)}$ at a C/20 rate until reaching a −0.6 V versus Ag/AgCl voltage cutoff. *C/N* describes the current to (de)intercalate the electrode in *N*h. The active material mass loading on the counter electrodes ranged between 60 and 70 $mg{\cdot}cm^{-2}$. To measure the capacity, the $FePO_4$ electrodes were cycled at 14.7 $mA{\cdot}g^{-1}$ between −0.6 and 0.6 V (vs. Ag|AgCl|saturated KCl), which gives us 147 $mAh{\cdot}g^{-1}$ specific capacity (*SI Appendix*, Fig. S3).

Electrochemical Methods. All electrochemical operations were performed on a Bio-Logic VMP3 workstation using a three-neck round-bottomed flask in the N_2 atmosphere with Ag|AgCl|KCl (saturated) as the reference electrode.

CV tests with voltages ranging from −0.6 V to 0.6 V (vs. Ag|AgCl|saturated KCl) for the $FePO_4$ hosts are performed in 1 M LiCl/NaCl/KCl/$MgCl_2$/$CaCl_2$ aqueous solution under the scan rate of 0.03 mV/s.

For the Li^+ capturing process in binary/ternary/simulated brine solutions, $FePO_4$ working electrodes, paired with $NaFePO_4$ counter electrodes, undergo intercalation in 500 mL of target solutions until 50% of the total capacity, using different intercalation C rates (14.7 mA/g equals a rate of 0.1 C; *SI Appendix*, Fig. S3). The molar concentration of Li^+ in the mixed solutions is fixed at 1 mM unless specified.

For the Li^+ releasing process in the recovery solution, after finishing the Li^+ capturing process, the electrode was first rinsed in three different 60 mL of DI water for 30 min with continuous N_2 bubbling to remove excess adsorbed cations. The electrode was then deintercalated in 30 mM NH_4HCO_3 aqueous solution under a C/40 constant current, using a graphite rod (Sigma-Aldrich, 99.995%) as the counter electrode. The solution before and after the deintercalation process was collected for ICP-MS for ion concentration measurement.

The FE_{Li} is described as the percentage of the charge flow that is effectively used to extract Li^+, and it is expressed as follows (21):

$$F.E._{Li} = \frac{F\Delta C_{Li}V}{Q},$$

where F is the Faraday constant, V is the volume of the recovery solution, ΔC_{Li} is the Li^+ concentration difference in the recovery solution before and after the deintercalation process, and Q is the total charge flow during the Li extraction step.

Another indicator is the Li selectivity, which is defined by the following equation:

$$\eta_{Li-M1} = \frac{([Li]/[M1])_{final}}{([Li]/[M1])_{initial}}.$$

For Stepconc CP tests in binary or ternary solutions, we fixed the concentration of interfering ions at 1 M while constantly changing the concentration of $[Li^+]$ in the beaker cell. The applied C rate is 0.1 C (14.7 mA/g) until 70% of the total capacity is used.

XRD Characterization. XRD was carried out on a Rigaku MiniFlex 600 diffractometer, using Cu Kα radiation (Kα 1: 1.54059 Å; Kα 2: 1.54441 Å; Kα 12 ratio: 0.4970). The tube voltage and the current used were 40 kV and 15 mA. Diffractograms were recorded with a 0.01° step width and a 5°/min speed.

ICP-MS Characterization. Three percent $HNO_{3(aq)}$ was used as the diluting matrix, and all the measurements used either Thermo iCAP Q ICP-MS or Thermo iCAP RQ ICP-MS.

Scanning Electron Microscopy Characterization. Scanning electron microscopy (Zeiss Merlin) was performed at the accelerating voltage of 10 kV.

OLS Regression. To predict the FE_{Li} in a Li–Na–Ca/Mg ternary solution, we implement the OLS method of linear regression. A linear model of the form is proposed below, where $\hat{y}_i$ is the predicted FE_{Li} for the ternary solution *i*, $\mathbf{x}_i$ is a two-dimensional feature vector for the ternary solution *i*, which considers the Na:Li molar ratio and Mg:Li molar ratio for Li–Na–Mg ternary solutions (Na:Li and Ca:Li for Li–Na–Ca ternary solutions), and $\hat{\mathbf{w}}$ is a two-dimensional model coefficient vector for the two features,

$$\hat{y}_i = \hat{\mathbf{w}}^T\mathbf{x}_i.$$

The formulation is

$$\hat{\mathbf{w}} = \text{argmin}_{\mathbf{w}}\|\mathbf{y} - \mathbf{X}\mathbf{w}\|_2^2,$$

where the argmin function represents finding the value of $\mathbf{w}$ that minimizes the argument, $\mathbf{y}$ is the *n*-dimensional vector of tested FE_{Li}, and $\mathbf{X}$ is the $n \times 2$ matrix of features. The term $\|\mathbf{y} - \mathbf{X}\mathbf{w}\|_2^2$ is found in OLS. After finding the 2D model coefficient vector for the features, we can generate the predicted FE_{Li} color map in Fig. 5*A* and *B*.

Data Availability. All study data are included in the article and/or *SI Appendix*. Any raw experimental data will be made available upon reasonable request to the authors.

ACKNOWLEDGMENTS. We thank Yiheng Wu (University of Chicago) for the insightful discussions on OLS regression. This work is supported by the Pritzker School of Molecular Engineering at the University of Chicago and partially supported by the University of Chicago Materials Research Science and Engineering Center, which is funded by the NSF under Award DMR-2011854.

1. Roskill, *Lithium-Ion Batteries Outlook to 2028* (Roskill, London, ed. 3, 2019).
2. P. Greim, A. A. Solomon, C. Breyer, Assessment of lithium criticality in the global energy transition and addressing policy gaps in transportation. *Nat. Commun.* **11**, 4570 (2020).
3. C. Grosjean, P. H. Miranda, M. Perrin, P. Poggi, Assessment of world lithium resources and consequences of their geographic distribution on the expected development of the electric vehicle industry. *Renew. Sustain. Energy Rev.* **16**, 1735–1744 (2012).
4. B. Swain, Recovery and recycling of lithium: A review. *Separ. Purif. Tech.* **172**, 388–403 (2017).
5. S. Yang, F. Zhang, H. Ding, P. He, H. Zhou, Lithium metal extraction from seawater. *Joule* **2**, 1648–1651 (2018).
6. Z. Li *et al.*, Continuous electrical pumping membrane process for seawater lithium mining. *Energy Environ. Sci.* **14**, 3152–3159 (2021).
7. E. R. Nightingale, Phenomenological theory of ion solvation. Effective radii of hydrated ions. *J. Phys. Chem.* **63**, 1381–1387 (1959).
8. D. W. Smith, Ionic hydration enthalpies. *J. Chem. Educ.* **54**, 540 (1977).
9. S. Nishimura *et al.*, Experimental visualization of lithium diffusion in Li_xFePO_4. *Nat. Mater.* **7**, 707–711 (2008).
10. S. P. Ong *et al.*, Voltage, stability and diffusion barrier differences between sodium-ion and lithium-ion intercalation materials. *Energy Environ. Sci.* **4**, 3680–3688 (2011).
11. M. Pasta, A. Battistel, F. La Mantia, Batteries for lithium recovery from brines. *Energy Environ. Sci.* **5**, 9487–9491 (2012).
12. J.-S. Kim *et al.*, An electrochemical cell for selective lithium capture from seawater. *Environ. Sci. Technol.* **49**, 9415–9422 (2015).
13. C. Liu *et al.*, Lithium extraction from seawater through pulsed electrochemical intercalation. *Joule* **4**, 1459–1469 (2020).
14. C. Delmas, M. Maccario, L. Croguennec, F. Le Cras, F. Weill, Lithium deintercalation in $LiFePO_4$ nanoparticles via a domino-cascade model. *Nat. Mater.* **7**, 665–671 (2008).
15. Y. Z. Dong, Y. M. Zhao, H. Duan, Crystal structure and lithium electrochemical extraction properties of olivine type $LiFePO_4$. *Mater. Chem. Phys.* **129**, 756–760 (2011).
16. Z. Rong *et al.*, Materials design rules for multivalent ion mobility in intercalation structures. *Chem. Mater.* **27**, 6016–6021 (2015).
17. M. Li *et al.*, Design strategies for nonaqueous multivalent-ion and monovalent-ion battery anodes. *Nat. Rev. Mater.* **5**, 276–294 (2020).

18. R. Trócoli, A. Battistel, F. L. Mantia, Selectivity of a lithium-recovery process based on $LiFePO_4$. *Chemistry* **20**, 9888–9891 (2014).
19. X. Liu, X. Chen, Z. Zhao, X. Liang, Effect of Na^+ on Li extraction from brine using $LiFePO_4/FePO_4$ electrodes. *Hydrometallurgy* **146**, 24–28 (2014).
20. N. Intaranont, N. Garcia-Araez, A. L. Hector, J. A. Milton, J. R. Owen, Selective lithium extraction from brines by chemical reaction with battery materials. *J. Mater. Chem. A Mater. Energy Sustain.* **2**, 6374–6377 (2014).
21. A. Battistel, M. S. Palagonia, D. Brogioli, F. La Mantia, R. Trócoli, Electrochemical methods for lithium recovery: A comprehensive and critical review. *Adv. Mater.* **32**, e1905440 (2020).
22. M. S. Palagonia, D. Brogioli, F. La Mantia, Lithium recovery from diluted brine by means of electrochemical ion exchange in a flow-through-electrodes cell. *Desalination* **475**, 114192 (2020).
23. T. Han *et al.*, Green recovery of low concentration of lithium from geothermal water by a novel FPO/KNiFC ion pump technique. *Electrochim. Acta* **350**, 136385 (2020).
24. G. T. Hill, F. Shi, H. Zhou, Y. Han, C. Liu, Layer spacing gradient $(NaLi)_{1-x}CoO_2$ for electrochemical Li extraction. *Matter* **4**, 1611–1624 (2021).
25. I. Warren, "Techno-economic analysis of lithium extraction from geothermal brines" (Rep. NREL/TP-5700-79178, National Renewable Energy Laboratory, Golden, CO, 2021).
26. US Environmental Protection Agency, "Technical development document for the effluent limitations guidelines and standards for the oil and gas extraction point source category" (Rep. 820-R-16-003, US Environmental Protection Agency, 2016).
27. J. Veil, *U.S. Produced Water Volumes and Management Practices in 2017* (National Ground Water Research and Educational Foundation, 2020).
28. E. Jones, M. Qadir, M. T. H. van Vliet, V. Smakhtin, S. M. Kang, The state of desalination and brine production: A global outlook. *Sci. Total Environ.* **657**, 1343–1356 (2019).
29. L. Li *et al.*, Lithium recovery from aqueous resources and batteries: A brief review. *Johnson Matthey Technol. Rev.* **62**, 161–176 (2018).
30. US Geological Survey, U.S. Geological Survey National Produced Waters Geochemical Database (ver. 2.3). https://www.usgs.gov/data/us-geological-survey-national-produced-waters-geochemical-database-v23. Accessed 9 January 2018.
31. US Geological Survey, USGS Open File Database for Geothermal Brines.
32. A. K. Padhi, K. S. Nanjundaswamy, J. B. Goodenough, Phospho-olivines as positive-electrode materials for rechargeable lithium batteries. *J. Electrochem. Soc.* **144**, 1188–1194 (1997).
33. Y. Zhu, Y. Xu, Y. Liu, C. Luo, C. Wang, Comparison of electrochemical performances of olivine $NaFePO_4$ in sodium-ion batteries and olivine $LiFePO_4$ in lithium-ion batteries. *Nanoscale* **5**, 780–787 (2013).
34. P. Moreau, D. Guyomard, J. Gaubicher, F. Boucher, Structure and stability of sodium .intercalated phases in olivine $FePO_4$. *Chem. Mater.* **22**, 4126–4128 (2010).
35. J. C. Lu, S. C. Chung, S. Nishimura, A. Yamada, Phase diagram of olivine Na_xFePO_4 ($0 < x < 1$). *Chem. Mater.* **25**, 4557–4565 (2013).
36. G. Oyama, S.-i. Nishimura, S.-C. Chung, M. Okubo, A. Yamada, Electrochemical properties of heterosite $FePO_4$ in aqueous Mg^{2+} electrolytes. *Electrochemistry (Tokyo)* **82**, 855–858 (2014).
37. R. Zhang, C. Ling, Unveil the chemistry of olivine $FePO_4$ as magnesium battery cathode. *ACS Appl. Mater. Interfaces* **8**, 18018–18026 (2016).
38. T. F. Fuller, J. N. Harb, *Electrochemical Engineering* (Wiley, Hoboken, NJ, 2018).
39. M. S. Palagonia, D. Brogioli, F. La Mantia, Effect of current density and mass loading on the performance of a flow-through electrodes cell for lithium recovery. *J. Electrochem. Soc.* **166**, E286–E292 (2019).
40. S. Kim *et al.*, High-voltage phosphate cathodes for rechargeable Ca-ion batteries. *ACS Energy Lett.* **5**, 3203–3211 (2020).
41. M. A. Brown *et al.*, Determination of surface potential and electrical double-layer structure at the aqueous electrolyte-nanoparticle interface. *Phys. Rev. X* **6**, 011007 (2016).
42. I. Ledezma-Yanez *et al.*, Interfacial water reorganization as a pH-dependent descriptor of the hydrogen evolution rate on platinum electrodes. *Nat. Energy* **2**, 17031 (2017).
43. J. Li, X. Li, C. M. Gunathunge, M. M. Waegele, Hydrogen bonding steers the product selectivity of electrocatalytic CO reduction. *Proc. Natl. Acad. Sci. U.S.A.* **116**, 9220–9229 (2019).
44. Y.-H. Wang *et al.*, In situ Raman spectroscopy reveals the structure and dissociation of interfacial water. *Nature* **600**, 81–85 (2021).
45. Y. Li *et al.*, Fluid-enhanced surface diffusion controls intraparticle phase transformations. *Nat. Mater.* **17**, 915–922 (2018).